Determining the Gas-Phase Structures of α-Helical Peptides: Insights from Shape, Intramolecular Distance, and Microsolvation Assays

Working Paper

Author(s):
Wu, Ri; Metternich, Jonas B.; Kamenik, Anna S.; Tiwari, Prince; Harrison, Julian A.; Kessen, Dennis; Akay, Hasan; Benzenberg, Lukas R.; Chan, T.-W. Dominic; Riniker, Sereina; Zenobi, Renato

Publication date:
2023-04-06

Permanent link:
https://doi.org/10.3929/ethz-b-000606813

Determining the Gas-Phase Structures of α-Helical Peptides: Insights from Shape, Intramolecular Distance, and Microsolvation Assays

Ri Wu,[1‡] Jonas B. Metternich,[1‡] Anna S. Kamenik,[2‡] Prince Tiwari,[1,4] Julian A. Harrison,[1] Dennis Kessen,[1,5] Hasan Akay,[1] Lukas R. Benzenberg,[1] T.-W. Dominic Chan,[3] Sereina Riniker,[2*] and Renato Zenobi[1*]

Mass spectrometry is a powerful technique for the structural and functional characterization of biomolecules. However, it remains challenging to accurately probe the gas-phase structure of biomolecular ions. In this work, we propose a new, synergistic approach which utilizes ion mobility-mass spectrometry, Förster resonance energy transfer, and differential ion mobility spectrometry to provide multiple constraints for molecular modelling of gas-phase ion structures. This combined strategy showed superb capabilities for distinguishing conformers and was employed to understand the gas-phase structures of two isomeric α-helical peptides that might differ in helicity. Shape and intramolecular distance constraints were included in structure-refinement calculations after an extensive conformational search. We added microsolvation calculations to assess the interaction sites and energies between the peptide ions and the gaseous additives, which confirmed differences in experimentally observed differential mobilities. Our work allows more rigorous and comprehensive structural characterization of biomolecular ions in the gas phase.

Soft ionization techniques[1,2] for mass spectrometry (MS) are thought to retain the structural characteristics of biomolecules when transferred from solution into the gas phase.[3,4] This has been termed 'native MS' and is used to determine the stoichiometry of noncovalent complexes, binding constants, melting temperatures[5–7], thermodynamics[8], and folding kinetics[9]. MS data can be combined with computational studies for structural analysis, for example, in studies of hydrogen–deuterium exchange[10], chemical cross-linking[11], covalent labeling methods[12], or surface-induced dissociation (SID)[13]. More recently, MS has been coupled to structural probes, such as circular dichroism, ion mobility spectrometry or fluorescence spectroscopy, more specifically Förster resonance energy transfer (FRET), to provide insights into the conformations of biomolecular ions.[14–17] Such studies are complicated, and normally only an isolated structural methodology was applied.

Ion mobility-mass spectrometry (IM-MS) is the most common method to investigate the geometry of gas-phase ions. In IM-MS, ions undergo collisions with a neutral gas (e.g., He, N_2) and are separated according to the so-called zero-field mobility coefficients, $K(0)$. At low electric field strengths, $K(0)$ can be considered a constant. The collisional cross section (CCS), referring to the rotationally-averaged surface area available for collisions, can be calculated directly or obtained from the arrival time distribution after calibration. The CCS can then be used to model possible conformations. Unlike IM-MS, FRET measurements are based on the distance dependence of a radiation-free transfer of energy from a donor chromophore to an acceptor chromophore.[18] With the knowledge of the chromophores' binding sites within a molecule and their photo-physical properties, intramolecular distances can be measured. FRET is commonly used to investigate the structure of biomolecules in solution; in the gas phase, FRET measurements are usually challenging due to low ion density and inefficient fluorescence collection.[17] However, the ability to perform conformational studies in a controlled chemical environment (i.e., a solvent-free environment, high purity, and selected charge states) is very interesting for determining the gaseous structure of biomolecular ions.

FRET measurements in the gas phase are now becoming feasible, yet the acquired structural information is still insufficient for obtaining comprehensive geometrical information.[19–21] Similarly, IM-MS alone provides limited conformational information if multiple species (i.e., conformations) are indistinguishable. IM-MS has been coupled with other techniques, e.g., cryogenic ion spectroscopy, for accurate gas-phase structural

[1]Laboratorium für Organische Chemie, ETH Zürich, D-CHAB, 8093 Zurich, Switzerland. [2]Laboratorium für Physikalische Chemie, ETH Zürich, D-CHAB, 8093 Zurich, Switzerland. [3]Department of Chemistry, The Chinese University of Hong Kong, Hong Kong SAR, People's Republic of China. Present addresses: [4]Laboratory of Atmospheric Chemistry, Paul Scherrer Institute, Forschungsstrasse 111, 5232 Villigen PSI, Switzerland. [5]University of Münster, MEET Battery Research Center, Corrensstrasse 46, 48149 Münster, Germany.
[‡]These authors contributed equally.
Email: sriniker@ethz.ch; zenobi@org.chem.ethz.ch

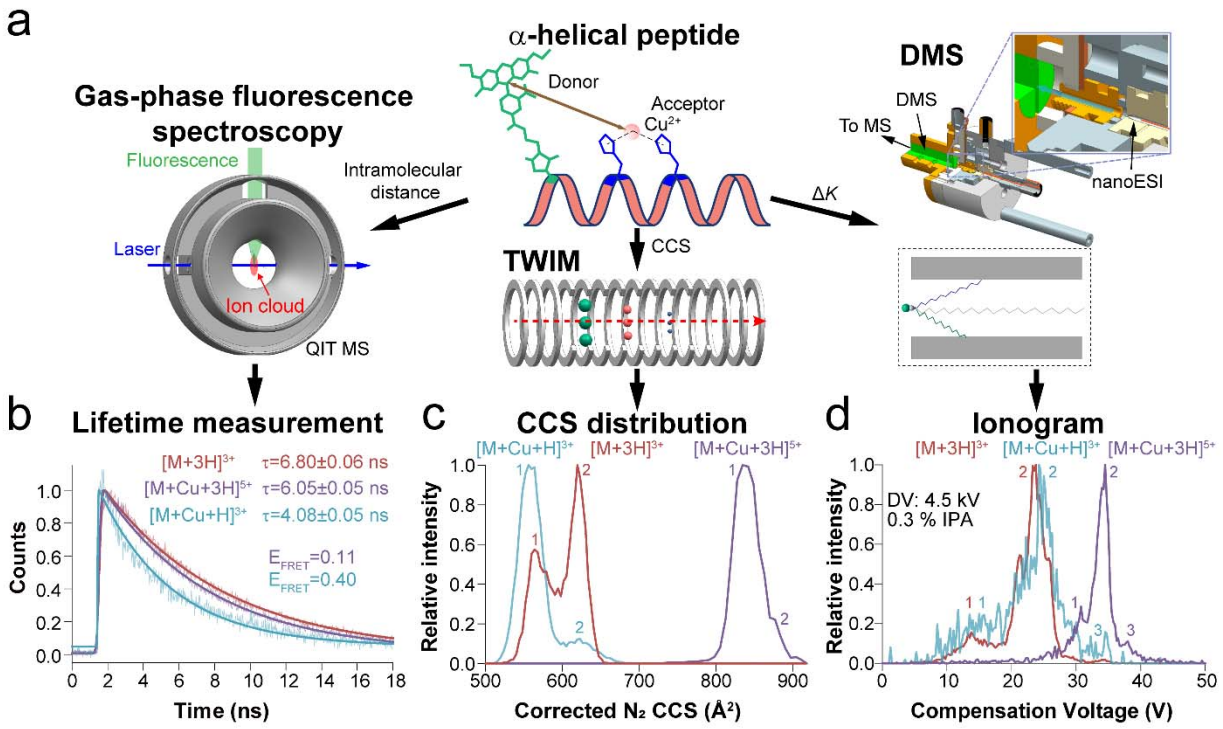

Fig. 1 | Structural characterization of an α-helical peptide in the gas phase. a, Overview of the structural characterization approach. **b**, Lifetime decay curves, **c**, Traveling wave ion mobility (TWIM) CCS distributions, and **d,** DMS ionograms of the $[M+3H]^{3+}$, $[M+H+Cu]^{3+}$, and $[M+3H+Cu]^{5+}$ ions of cR6G-tm**P1**.

characterization of biomolecular ions in combination with molecular dynamic simulations.[22–25] Reports on coupling of IM-MS and FRET are sparse. Modifications of a drift tube IM-MS instrument for laser excitation and action-FRET experiments have been reported.[26,27] In action-FRET, the FRET efficiency is determined by the photo-fragmentation yield of the acceptor[28], thus this approach is not compatible with fluorescence detection and classical FRET.

The combination of FRET and IM-MS was recently shown to greatly aid simulations to determine ion structures in the gas phase.[29] To further develop this approach, here we introduce a coupling of differential ion mobility spectrometry (DMS) to resolve species prior to FRET and IM-MS measurements. Orthogonal to IM-MS, gas-phase ions in DMS are separated based on their differential mobility (ΔK) between low- and high-fields in atmospheric pressure.[30] DMS separation is related to many physicochemical properties of ions, including microsolvation, the rate of clustering/ declustering, and the ion-modifier binding energy.[31–36] We hypothesize that combining shape and distance constraints from IM-MS and FRET with microsolvation information from DMS data and molecular modeling would be much more powerful and precise for determining gas-phase conformations (Figure 1a).

Results and discussion

Structural evaluation of an α-helical peptide using FRET, IM-MS, and DMS. As a proof of concept, we first investigated an alanine rich α-helical peptide labeled with carboxyrhodamine 6g (cR6G) using the proposed method (cR6G-tm**P1**, scheme S1). Transition metal ion FRET (tmFRET) is a recent extension of FRET experiments in the gas phase, which enables the measurement of short biomolecular backbone distances (e.g., 10–40 Å).[37] Cu^{2+} serves as an acceptor chromophore and binds noncovalently to a His-X_3-His motif (X refers to any amino acid), which simplifies the dye labeling for FRET measurements. The results showed FRET efficiencies (E_{FRET}) of 0.40 and 0.11 for the $[M+Cu+H]^{3+}$ and $[M+Cu+3H]^{5+}$ ions of cR6G-tm**P1**, respectively (Figures 1b and S1). The predicted gas-phase Förster radius ($R_{0,\,gas}$) for the dye and Cu^{2+} pair is 26.0 Å (refer to Methods), and the estimated donor-acceptor distances (r_{DA}) are 27.8 ± 0.3 Å for $[M+H+Cu]^{3+}$ ions, and 36.8 ± 0.8 Å for $[M+3H+Cu]^{5+}$ ions.

However, it is known that multiple conformations can lead to overlapping fluorescence decay curves, which require multiple-exponential fits (Table S1). Here, only the $[M+H+Cu]^{3+}$ ion showed two lifetime values of 0.64 (i.e., compact conformation) and 5.99 ns (i.e., expanded conformation). IM-MS results also indicated the existence of two major conformers for the $[M+H+Cu]^{3+}$ ion (Figures 1c and S2a-b). IM-MS measurements on other α-helical peptides (i.e., tm**P2**, tm**P3**, and tm**P4** labelled with rhodamine 110) also showed the existence of multiple conformations (Figures S2a-b, and Table S2). The results highlight the necessity of multiple structural probes in the gas phase.

The corresponding DMS results of cR6G-tm**P1**, rh110-tm**P2**, -tm**P3**, and -tm**P4** (i.e., rh110 labeled to cysteine 2) ions exhibited orthogonal conformational information to IM-MS (Figures 1d, S2c-d, and S4-S12). Therefore, DMS could: i. potentially disentangle the complexity of multiple gas-phase structures by separation of conformations; ii. add another dimension for the analysis of gas-phase structures

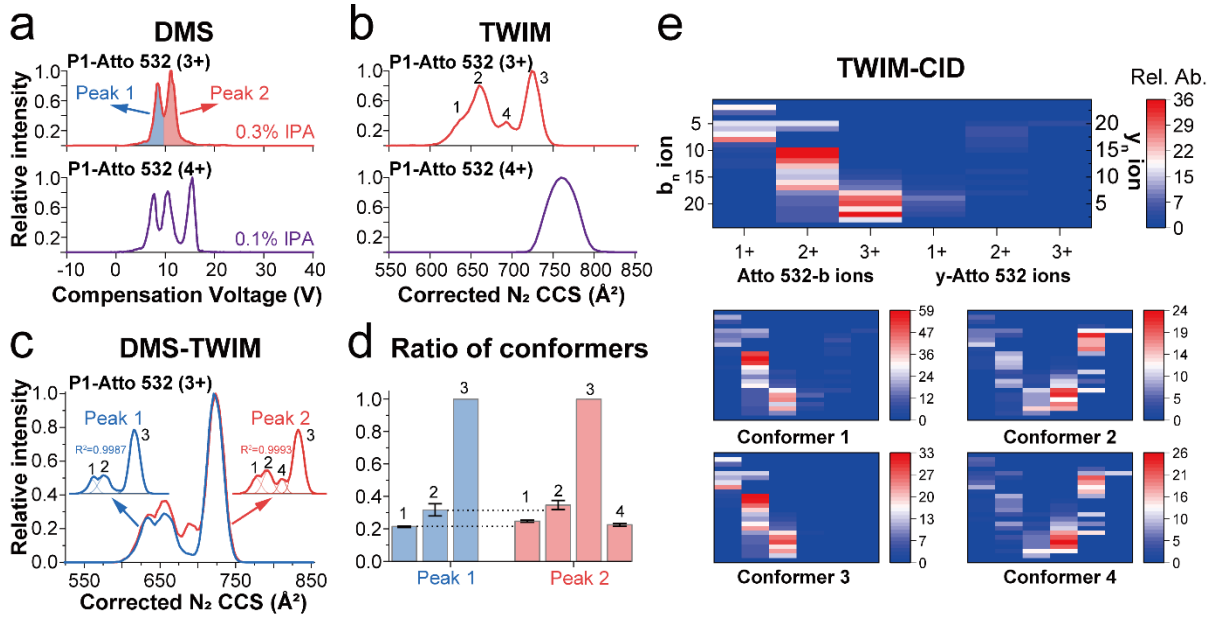

Fig. 2 | Conformational characterization of a mixture of dye-labeled peptide isomers. a, DMS ionograms (i.e., spectra), and **b**, TWIM CCS distributions of the $[M+3H]^{3+}$ and $[M+4H]^{4+}$ ions of **P1**-Atto 532/Atto 532-**P1** mixture. **c**, TWIM CCS distributions of the $[M+3H]^{3+}$ ion in the DMS-TWIM measurements. Compensation voltage (CV) was set to 8 V and 10.25 V for peak 1 and peak 2, respectively. **d**, The peak ratio of conformers extracted from 2c and differentiated from the DMS-TWIM measurements. **e**, TWIM-CID experiments for all (top) and each conformer (bottom). Diagnostic b/y fragment ions with the dye attached to the N- or C-terminal cysteine are presented in the heat map. Relative abundances are normalized to the intensity of the $[M+3H]^{3+}$ ion (i.e., precursor ion).

by providing additional physicochemical information (i.e., microsolvation and cluster formation).

DMS separation of a mixture of dye-labeled α-helical peptide isomers. To test the performance of a home-built DMS device (Figure S13) and its coupling to IM-MS and fluorescence spectroscopy, we turned to a polyalanine-based α-helical peptide with the sequence Ac-*C*AAAHAAAHAAAAHAAAHAAA*C*AK-NH_2 (**P1**). The distance between the two cysteines were optimized to fit for the measurements of large biomolecular backbone distances by traditional FRET. It was then singly labelled using an Atto 532 dye with a maleimide linker. The dye was covalently attached to one of the available cysteine residues (scheme S1). The two labeling-site isomers (**P1**-Atto 532/Atto 532-**P1**) could not be separated by HPLC (Figure S14), therefore all experiments were performed using the mixture. Isopropanol (IPA), a common gaseous additive (i.e., gas modifier), was added into the carrier gas to enhance the separation (Figures S15-S16). The DMS separation yielded two peaks for the $[M+3H]^{3+}$ ion and three peaks for the $[M+4H]^{4+}$ ion at IPA concentrations of 0.3 mol % and 0.1 mol %, respectively (Figure 2a).

DMS coupled to fluorescence spectroscopy and IM-MS for characterization of isomers and conformers. Fluorescence spectroscopic measurements were used to examine the structural difference between the two $[M+3H]^{3+}$ ion populations (assigned as peak 1 and 2) of **P1**-Atto 532/Atto 532-**P1** isomers after DMS separation (Figure 2a). The emission spectra of peak 1 and 2 showed identical maxima and shape (Figure S17). Comparison of the emission spectra obtained for the 3+ and 4+ charge states revealed a blue shift of the emission maximum from 535.5 nm to 528.5 nm (Figure S18). The altered emission properties are likely due to changes in the solvation environment of the dye or the additional charge interacting with the fluorophore's dipole. To characterize peaks 1 and 2, collision-induced dissociation (CID) and photodissociation were also conducted after DMS (Figures S19-S20). Since the dye is located on either the N- or C-terminal cysteine in the mixture, it is possible to identify which dye configuration is present based on the sequence data generated via fragmentation. However, the two DMS peaks for the $[M+3H]^{3+}$ ions gave fragment ions for both labelling site isomers.

The CCS distributions of the $[M+3H]^{3+}$ and $[M+4H]^{4+}$ ions of **P1**-Atto 532/Atto 532-**P1** were measured by traveling wave ion mobility (TWIM) to obtain a better understanding of the gas-phase conformation of these ions. The CCS distribution of the $[M+3H]^{3+}$ ion contained four ion populations (assigned as conformers 1 to 4), showing that these ions can adopt multiple conformations in the gas phase. The $[M+4H]^{4+}$ ion exhibited a single, broad CCS distribution (Figure 2b). Experimental average CCS values of each conformer are given in Table S3.

To further explore the DMS–IM-MS method, peaks 1 and 2 of the $[M+3H]^{3+}$ ion observed in the DMS ionogram were investigated using TWIM. Figure 2c shows the CCS distributions for the $[M+3H]^{3+}$ ion populations after DMS separation. Using a compensation voltage (CV) of ~8 V (i.e., peak 1), three conformers were detected by TWIM, while four conformers were detected when the CV was set to ~10.25 V (i.e., peak 2). In both cases, conformer 3 was the most abundant and had the highest CCS value of all the observed conformational variants. This indicates that most $[M+3H]^{3+}$ ions correspond to expanded structures. The relative intensity of conformers 1 and 2 are slightly lower in peak 1 than peak 2. An ion population with a CCS of ~ 690 Å², labeled "conformer 4", was only found in peak 2 and could be isolated using DMS (Figure 2d).

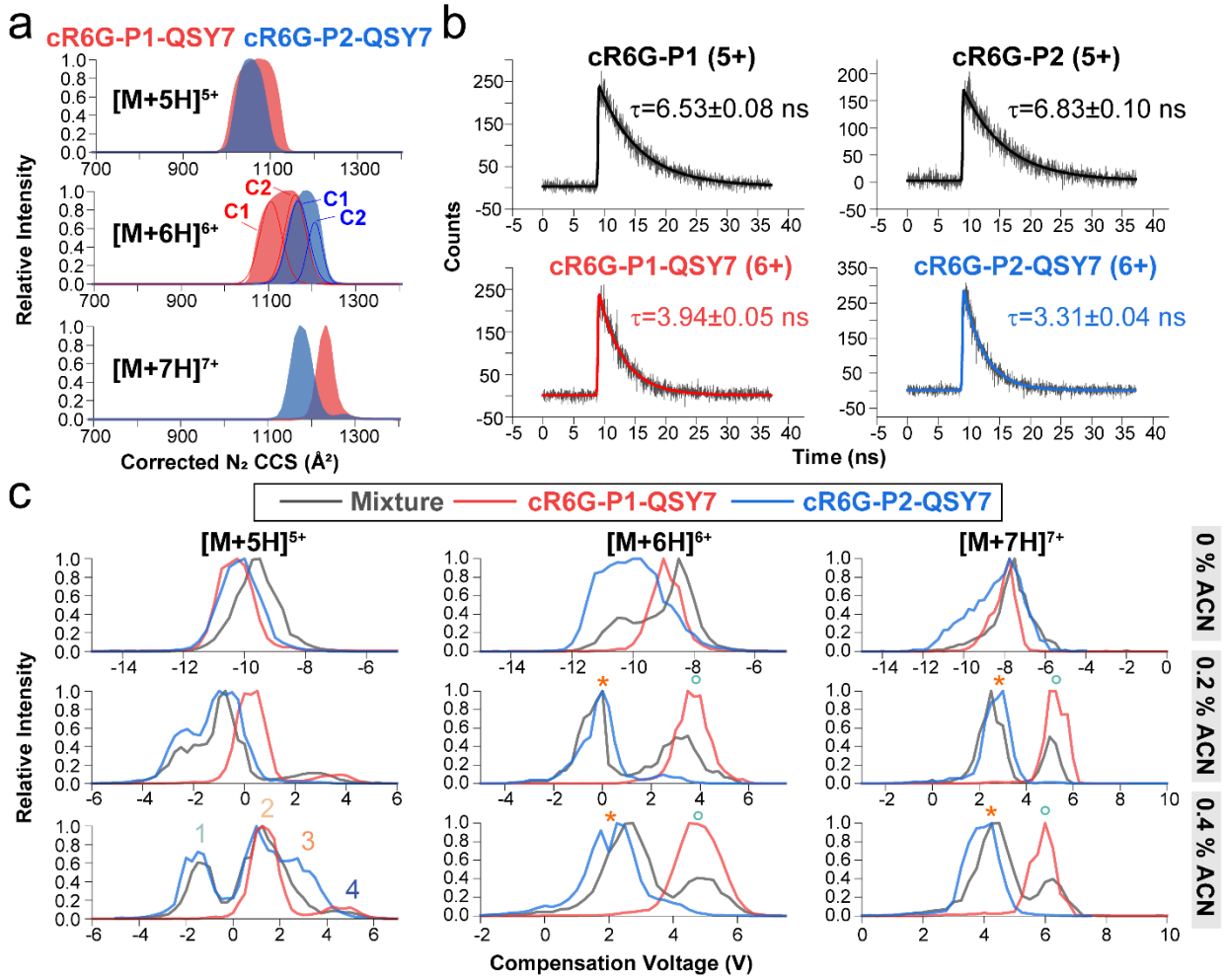

Fig. 3 | Structural characterization of two isomeric α-helical peptides in the gas phase. a, Normalized TWIM CCS distributions of cR6G-**P1**-QSY7 and cR6G-**P2**-QSY7 ions in a 7.5 V wave height. **b**, Lifetime decay curves of the $[M+5H]^{5+}$ ions of cR6G-**P1** and cR6G-**P2**, and the $[M+6H]^{6+}$ ions of cR6G-**P1**-QSY7 and cR6G-**P2**-QSY7. **c**, DMS ionograms of cR6G-**P1**-QSY7 and cR6G-**P2**-QSY7 ions in 0, 0.2, and 0.4 mol % acetonitrile (ACN) as the gas modifier.

Since the conformers could not be identified by DMS and CID, further sequencing experiments were conducted after TWIM separation (Figure S22). CID mass spectra were acquired for all of the four conformers (top) and each conformer (bottom) of the $[M+3H]^{3+}$ ion. b/y fragment ions were identified during these experiments, with charge states ranging from 1+ to 3+, with/without the dye in the N- or C- terminal cysteines (Tables S4-S8). Two labeling-site isomers are expected to show diagnostic b or y fragment ions with the dye labeled. The diagnostic fragment ions are shown as heat maps in Figure 2e. A higher ratio of Atto 532-b ions (i.e., b ions with the dye on the N-terminal cysteine) was found overall (top), which likely suggests that there is a relatively higher ratio of Atto 532-**P1** in the mixture. Remarkably, conformers 1 and 3 indicated a high ratio of Atto 532-b ions, while conformers 2 and 4 indicated a high ratio of y-Atto 532 ions (i.e., y ions with the dye on the C-terminal cysteine). The relatively low ratio of y-Atto 532 ions for conformers 1 and 3, and Atto 532 ions-b ions for conformers 2 and 4 are likely due to partially overlapped peaks in the CCS distributions. The TWIM-CID results of the $[M+3H]^{3+}$ ion suggest that conformers 1 and 3 correspond to the Atto 532-**P1** isomers, while conformers 2 and 4 originate from the **P1**-Atto 532 isomers. The ratios of the four conformers were slightly different between experiments, which is dependent on the ratios of isomers collected from different HPLC batches. Overall, several coexisting conformers were differentiated and could be assigned to the respective isomers. The improved selectivity and the ability to couple the DMS to different instruments demonstrate the power and utility of such an orthogonal approach.[38,39]

Structural elucidation of the two isomeric α-helical peptides with IM-MS and FRET. To test the new approach, the same isomeric α-helical peptides (i.e., **P1** and **P2**) were chosen and labeled with cR6G and QSY7 as donor fluorophore and acceptor chromophore, respectively. The sequence of **P2** was (scheme S1) Ac-*KA*CAAAHAAAHAAAAHAAAHAAAC-NH_2. Previous investigations on polyalanine-based peptides showed that a C-terminal lysine could stabilize an α-helix in the gas phase by favorably interacting with the macrodipole of the helix.[40–43] To verify this, we firstly conducted solution-phase FRET experiments of cR6G-**P1**-QSY7 and cR6G-**P2**-QSY7. The results showed two conformations from the double-exponential fits (Figure S24 and Table S9). cR6G-**P1**-QSY7

exhibited a slightly lower lifetime for both conformations, as well as a higher ratio of molecules adopting compact conformations (58%) compared to cR6G-**P2**-QSY7 (40%). The results suggest that cR6G-**P1**-QSY7, which has a C-terminal lysine, maintains a high percentage of its helical structure in the solution.

The mass spectra acquired in native conditions showed that the dominant peak of the two doubly labelled peptides is the $[M+6H]^{6+}$ ion (Figure S26). TWIM separations showed partial separation of the conformational populations for these charge states (Figures 3a and S27). Two conformers were assigned to the $[M+6H]^{6+}$ ions of each peptide (Table S10). The experimentally-averaged CCS values of the $[M+6H]^{6+}$ ion of cR6G-**P1**-QSY7 are smaller than these of cR6G-**P2**-QSY7, which indicates that the former ion is more compact.

Gas-phase FRET was then conducted to acquire complementary structural information. Specifically, lifetime measurements of the $[M+6H]^{6+}$ ions of cR6G-**P1**-QSY7 and cR6G-**P2**-QSY7 were compared with lifetime data from the $[M+5H]^{5+}$ ions of cR6G-**P1** and cR6G-**P2** (Figure 3b). These two charge states exhibit the same number of charges on the peptide chain, as QSY7 is likely singly charged. The decay curves were fitted with a exponentially modified Gaussian function (Table S11). Only one conformation was identified for the $[M+6H]^{6+}$ ions of both peptides from the double-exponential fit (Table S12). FRET efficiency (E_{FRET}) were calculated from the lifetime values (Figure 4a and Table S13). The $R_{0,\,gas}$ was estimated to be 72.2 Å (refer to Methods). Therefore, the experimental r_{DA} values of the $[M+6H]^{6+}$ ion of cR6G-**P1**-QSY7 and cR6G-**P2**-QSY7 are 77.5 ± 2.5 Å, and 71.5 ± 0.9 Å, respectively (Figure 4b). In summary, the IM-MS and FRET results gave contradictory results regarding the compactness of the two isomers, showcasing the drawbacks of relying on a single structural probe.

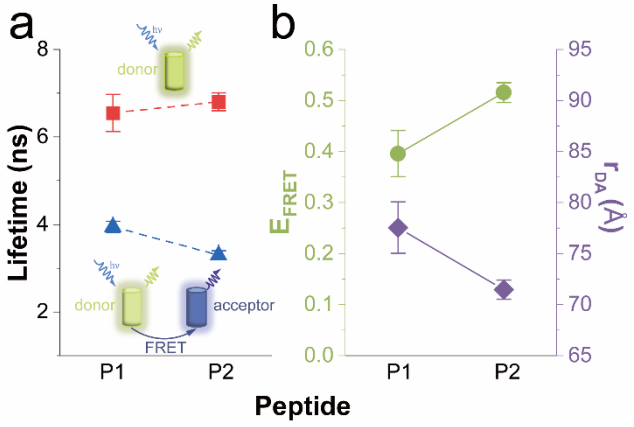

Fig. 4 | FRET experiments of two isomeric α-helical peptides in the gas phase. a, The lifetime values of the $[M+5H]^{5+}$ ions of cR6G-**P1** and cR6G-**P2** (red), and the $[M+6H]^{6+}$ ions of cR6G-**P1**-QSY7 and cR6G-**P2**-QSY7 (blue). **b**, FRET efficiencies (green) and r_{DA} values (purple) obtained from the lifetime measurements.

Using geometrical constraints from IM-MS and FRET for computational studies to determine the gas-phase structures. Advanced molecular modeling was conducted under consideration of the geometrical (i.e., shape and distance) data from the IM-MS and FRET measurements as constraints. All simulations were carried out with the AmberTools21 simulation package[44] and the GROMACS 2020.5 simulation engine[45–47] using the Amber force fields 14SB.[48] An extensive conformational search was conducted via a simulated annealing protocol (see Methods for details), which led to 5000 structural models for each peptide. These structures were then refined based on their force field energies, experimental CCS values, and r_{DA} values (Figures 5a-b). r_{DA} is defined by the distance between two carbon atoms at the para-position (C9) in the xanthene of donor and acceptor dyes. For each peptide we selected 10 structures (5 structures per IM-MS conformer).

For cR6G-**P1**-QSY7, all selected structures exhibit calculated r_{DA} values lower than the experimental ones (Figure 5a). Therefore, the 5 structures which had the theoretical r_{DA} values closest to the experimental ones were selected for each conformer (Figure S32 and Table S14). Note that experimental r_{DA} values (77.5 Å) are higher than the average values of the selected 5 structures from these two IM-MS conformers (66.5 Å and 71.7 Å). This indicates an overestimation of 14.1% and 7.5% for the conformers 1 and 2 by the FRET measurements, respectively. This is in agreement with previous observations of an overestimation of the $R_{0,\,gas}$ and thus the experimental r_{DA} value in the gas phase.[20] These results also show that the average r_{DA} values and CCS values (i.e., CCS_TJM*) of conformer 2 are larger than these of conformer 1, which is likely due to an overall extension of conformer 2. However, only one conformation could be inferred from the lifetime decay curves (Tables S11-12), highlighting the low selectivity of the traditional FRET method and the utility of coupling to IM-MS for measurements.

Structural analysis of cR6G-**P2**-QSY7 ions was more complicated than of cR6G-**P1**-QSY7 (Figure 5b). Some candidate structures have higher r_{DA} values than the experimental value (71.5 Å). Two conditions were then applied: i. we required the FRET results to indicate a qualitatively shorter r_{DA} value for the $[M+6H]^{6+}$ ions of cR6G-**P2**-QSY7 than cR6G-**P1**-QSY7. ii. a small, but systematic overestimation of $R_{0,\,gas}$ in the gas phase. Therefore, 5 structures with a calculated r_{DA} value nearest to, but below, the experimental r_{DA} value were selected for each conformer (Figure S32 and Table S14). The average r_{DA} values of two conformers were 67.9 Å and 69.1 Å, which gives an overestimation of 12.3% and 10.8% for conformers 1 and 2 based on the FRET measurements, respectively.

Within these selected structural models, the average force field energy of conformer 1 was generally lower than conformer 2 for both peptides (Table S14). In Figure 5a-b we display the lowest energy structure from each conformer of the two peptides as representative structures (see pdb structures in Tables S15-18). Both peptides were predicted to have elongated structures, yet each contained unique features. The cR6G moiety is oriented away from the peptide chain in both peptides, while QSY7 either folded onto (cR6G-**P1**-QSY7) or away from the peptide backbone (cR6G-**P2**-QSY7). The results show that cR6G-**P1**-QSY7 ions exhibit an α-helix (**P1**C1) or minor turns (**P1**C2), while cR6G-**P2**-QSY7 ions show large turns or random coils. These structural differences lead to a reduction in CCS but higher r_{DA} values for cR6G-**P1**-QSY7 ions. These models

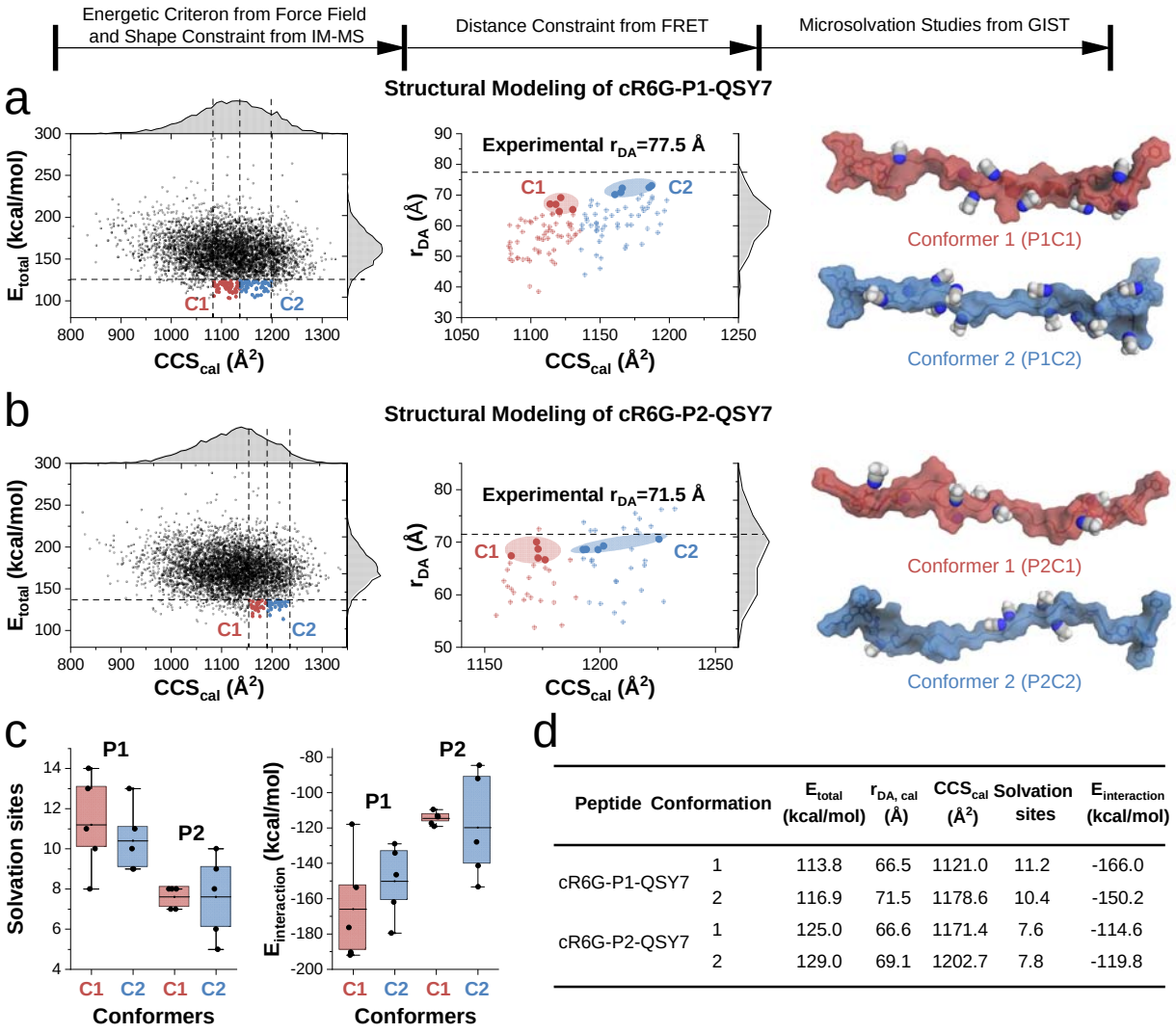

Peptide	Conformation	E_{total} (kcal/mol)	$r_{DA, cal}$ (Å)	CCS_{cal} (Å^2)	Solvation sites	$E_{interaction}$ (kcal/mol)
cR6G-P1-QSY7	1	113.8	66.5	1121.0	11.2	-166.0
	2	116.9	71.5	1178.6	10.4	-150.2
cR6G-P2-QSY7	1	125.0	66.6	1171.4	7.6	-114.6
	2	129.0	69.1	1202.7	7.8	-119.8

Fig. 5 | Computational simulations aid structural analysis of two isomeric α-helical peptides in the gas phase. a&b, Force field total energies (E_{total}) and CCS_{cal} values (defined as CCS_TJM* value from IMPACT) of 5000 candidate structures for the $[M+6H]^{6+}$ ion of cR6G-**P1**-QSY7 and cR6G-**P2**-QSY7. 20% energy cutoff, and experimental CCS values of conformer 1 (C1, red) and 2 (C2, blue) were applied to refine these structures. Further selection was achieved via experimental r_{DA} values for each IM-MS conformer. The representative structure (i.e., the lowest energy structure) from the refined 20 structures are presented with the solvation sites filled with ACN molecules. **c**, The number of solvation sites and interaction energies ($E_{interaction}$)of the $[M+6H]^{6+}$ ions are presented as box plots, where 5 structures per each cR6G-**P1**-QSY7 conformers have more solvation sites than cR6G-**P2**-QSY7 ions and consequently also more favorable interaction energies. The number of ACN molecules that cluster with the peptide ion depends on the available solvation sites. **d,** The calculated refinement parameters and microsolvation calculation results for the 5 refined structures per conformer (see SI).

hence already provide reasonable structural suggestions to interpret the seemingly opposing findings from the IM-MS and FRET experiments. In turn, this suggests that the combination of IM-MS and FRET can provide two complementary geometrical constraints (i.e., distance and shape) for molecular modeling, which enhance the understanding of peptide conformational ensembles in the gas phase. An improved accuracy of CCS measurements in IM-MS and a more accurate estimation of $R_{0, gas}$ could further facilitate the refinement of candidate structures.

Assessing refined structures with microsolvation information from DMS measurements. Another option to further test the reliability of our refined 20 structural models is to employ gas modifier-assisted DMS separations. The interaction potential (or binding energy) and dynamics of cluster formation, as well as the microsolvation states of charged molecules could be probed from the ions' behaviors in DMS.[34,49,50] In DMS, cR6G-**P1**-QSY7 and cR6G-**P2**-QSY7 ions could not be separated when using IPA as the gas modifier (Figure S33). Therefore, another commonly used gas modifier, ACN, was employed (Figures S34-S36). The resulting DMS ionograms showed good separation of the $[M+5H]^{5+}$, $[M+6H]^{6+}$, and $[M+7H]^{7+}$ ions in the presence of 0.2 or 0.4 mol % ACN (Figure 3c). The $[M+5H]^{5+}$ ions showed four peaks when using 0.4 mol % ACN as the gas modifier, of which peak 1 and 3 are likely originating only from cR6G-**P2**-QSY7. The $[M+6H]^{6+}$ and $[M+7H]^{7+}$ ions of the two peptides were nearly baseline-resolved. The results also revealed more ion-molecule clustering (i.e., cluster formation) for the $[M+6H]^{6+}$ ion of cR6G-**P1**-QSY7, which could then be assessed by microsolvation studies.

To model the microsolvation process in the gas phase, we then performed an in-depth analysis of the interaction potential of the 20 refined structures with ACN in the gas phase. Subtle differences in the structure will affect the solvation sites and interaction energies with ACN.[36] In a first step, we identified the most favorable interaction sites based on grid inhomogeneous solvation theory (GIST) calculations.[51,52] Based on the GIST predictions, we modeled the microsolvated complexes and calculated the solvation interaction energies. It was observed that ACN molecules interact strongly with the peptide backbone. The results indicated 10.8 most favorable solvation sites on average (11.2 for conformer 1, 10.4 for conformer 2) for the $[M+6H]^{6+}$ ion of cR6G-**P1**-QSY7. By comparison, 7.6 solvation sites on average (7.6 for both conformers) were found for cR6G-**P2**-QSY7 (Figures 5c-d and Table S14). As we modeled the peptide structures in complex with explicit ACN molecules, it was also possible to estimate the interaction energies. As expected we found significantly more favorable energies for the $[M+6H]^{6+}$ ion of cR6G-**P1**-QSY7. Conformers 1 and 2 of cR6G-**P1**-QSY7 on average showed an interaction energy of -166.0 kcal/mol and -150.2 kcal/mol respectively. For cR6G-**P2**-QSY7, the average interaction energies of -114.6 kcal/mol and -119.8 kcal/mol for conformers 1 and 2. In total, this results in average interaction energies of -158.1 kcal/mol and -117.2 kcal/mol for the $[M+6H]^{6+}$ ion of cR6G-**P1**-QSY7 and cR6G-**P2**-QSY7, respectively (Table S14). In addition, we followed an alternative modeling approach where we always included the positively charged cR6G and QSY7 as favorable interaction sites, resulting in average interaction energies of -175.8 kcal/mol and -137.2 kcal/mol, respectively (Table S19). Both strategies to model microsolvation revealed a more favorable cluster formation for the $[M+6H]^{6+}$ ion of cR6G-**P1**-QSY7. Consequently, a higher magnitude of cluster formation would induce a higher differential mobility (ΔK) in DMS separation. This would lead to a larger CV shift for the $[M+6H]^{6+}$ ion of cR6G-**P1**-QSY7 than cR6G-**P2**-QSY7 in DMS (Figures 3c and S34-S36). Hence, the agreement between the microsolvation calculations and the DMS experimental results provides further support for the 20 refined structures obtained when IM-MS and FRET data are used as structural constraints.

Conclusions

In this work, a differential ion mobility spectrometry (DMS) device was found to be sufficiently sensitive to allow for versatile hyphenated conformational analysis of isomers. We demonstrated the utility of using data obtained by multiple gas-phase techniques as constraints for molecular modeling. Intramolecular distances were determined by Förster resonance energy transfer (FRET), which served as a "molecular ruler". Ion mobility-mass spectrometry (IM-MS) measurements could determine collision cross sections (CCS) of gas-phase ions, providing information about the analytes gas-phase geometry. A conformational search was conducted to refine the gas-phase structures with distance constraints obtained from FRET measurements and shape constraints obtained from native IM-MS measurements. These filters significantly reduced the number of gas-phase structural models predicted from molecular modeling. The representative structures differ in the backbone helicity and acceptor chromophore folding between cR6G-**P1**-QSY7 and cR6G-**P2**-QSY7 ions. The results also allowed us to interpret the opposite indications from the IM-MS and FRET experiments.

Moreover, microsolvation calculations were conducted to acquire the number of solvation sites and interaction energy for these optimized structures. The results suggested a statistically significant difference between structures. The $[M+6H]^{6+}$ ion of cR6G-**P1**-QSY7 has more solvation sites and lower interaction energies on average. This is consistent with a more favorable cluster formation and therefore, a larger compensation voltage shift (i.e., higher ΔK) in the DMS. In conclusion, combining these three complementary experimental techniques with computational studies allows the determination of reliable conformational models of gas-phase biomolecular ions. This approach could be applied to other molecules (e.g., α-helix and β-sheet structures) or noncovalent complexes (e.g., protein-ligand complexes) to help obtain a better understanding of how ions behave in the gas phase, which is of fundamental importance to the field of native MS.

References

1. Fenn, J. B., Mann, M., Meng, C. K., Wong, S. F. & Whitehouse, C. M. Electrospray Ionization for Mass Spectrometry of Large Biomolecules. *Science (80-.).* **246**, 64–71 (1989).
2. Hillenkamp, F., Karas, M., Beavis, R. C. & Chait, B. T. Matrix-Assisted Laser Desorption/Ionization Mass Spectrometry of Biopolymers. *Anal. Chem.* **63**, 1193A-1203A (1991).
3. Heck, A. J. R. Native mass spectrometry: A bridge between interactomics and structural biology. *Nat. Methods* **5**, 927–933 (2008).
4. Leney, A. C. & Heck, A. J. R. Native Mass Spectrometry: What is in the Name? *J. Am. Soc. Mass Spectrom.* **28**, 5–13 (2017).
5. Benesch, J. L. P., Sobott, F. & Robinson, C. V. Thermal dissociation of multimeric protein complexes by using nanoelectrospray mass spectrometry. *Anal. Chem.* **75**, 2208–2214 (2003).
6. Wang, G., Abzalimov, R. R. & Kaltashov, I. A. Direct monitoring of heat-stressed biopolymers with temperature-controlled electrospray ionization mass spectrometry. *Anal. Chem.* **83**, 2870–2876 (2011).
7. El-Baba, T. J. *et al.* Melting Proteins: Evidence for Multiple Stable Structures upon Thermal Denaturation of Native Ubiquitin from Ion Mobility Spectrometry-Mass Spectrometry Measurements. *J. Am. Chem. Soc.* **139**, 6306–6309 (2017).
8. Marchand, A., Rosu, F., Zenobi, R. & Gabelica, V. Thermal Denaturation of DNA G-Quadruplexes and Their Complexes with Ligands: Thermodynamic Analysis of the Multiple States Revealed by Mass Spectrometry. *J. Am. Chem. Soc.* **140**, 12553–12565 (2018).
9. Marchand, A., Czar, M. F., Eggel, E. N., Kaeslin, J. & Zenobi, R. Studying biomolecular folding and binding using temperature-jump mass spectrometry. *Nat. Commun.* **11**, (2020).
10. Konermann, L., Pan, J. & Liu, Y. H. Hydrogen exchange mass spectrometry for studying protein structure and dynamics. *Chem. Soc. Rev.* **40**, 1224–1234 (2011).
11. Brodie, N. I., Popov, K. I., Petrotchenko, E. V., Dokholyan, N. V. & Borchers, C. H. Solving protein structures using short-distance cross-linking constraints as a guide for discrete molecular dynamics simulations. *Sci. Adv.* **3**, 3–26 (2017).
12. Aprahamian, M. L., Chea, E. E., Jones, L. M. & Lindert, S. Rosetta Protein Structure Prediction from Hydroxyl Radical Protein Footprinting Mass Spectrometry Data. *Anal. Chem.* **90**, 7721–7729 (2018).
13. Seffernick, J. T., Harvey, S. R., Wysocki, V. H. & Lindert, S. Predicting Protein Complex Structure from Surface-Induced Dissociation Mass Spectrometry Data. *ACS Cent. Sci.* **5**, 1330–1341 (2019).
14. Daly, S., Rosu, F. & Gabelica, V. Mass-resolved electronic circular dichroism ion spectroscopy. *Science (80-.).* **368**,

1465–1468 (2020).
15. Ruotolo, B. T., Benesch, J. L. P., Sandercock, A. M., Hyung, S. J. & Robinson, C. V. Ion mobility-mass spectrometry analysis of large protein complexes. *Nat. Protoc.* **3**, 1139–1152 (2008).
16. Lanucara, F., Holman, S. W., Gray, C. J. & Eyers, C. E. The power of ion mobility-mass spectrometry for structural characterization and the study of conformational dynamics. *Nat. Chem.* **6**, 281–294 (2014).
17. Czar, M. F. & Jockusch, R. A. Sensitive probes of protein structure and dynamics in well-controlled environments: Combining mass spectrometry with fluorescence spectroscopy. *Curr. Opin. Struct. Biol.* **34**, 123–134 (2015).
18. Kalinin, S. *et al.* A toolkit and benchmark study for FRET-restrained high-precision structural modeling. *Nat. Methods* **9**, 1218–1225 (2012).
19. Tiwari, P., Metternich, J. B., Czar, M. F. & Zenobi, R. Breaking the Brightness Barrier: Design and Characterization of a Selected-Ion Fluorescence Measurement Setup with High Optical Detection Efficiency. *J. Am. Soc. Mass Spectrom.* **32**, 187–197 (2021).
20. Talbot, F. O., Rullo, A., Yao, H. & Jockusch, R. A. Fluorescence resonance energy transfer in gaseous, mass-selected polyproline peptides. *J. Am. Chem. Soc.* **132**, 16156–16164 (2010).
21. Stockett, M. H., Houmøller, J., Støchkel, K., Svendsen, A. & Brøndsted Nielsen, S. A cylindrical quadrupole ion trap in combination with an electrospray ion source for gas-phase luminescence and absorption spectroscopy. *Rev. Sci. Instrum.* **87**, (2016).
22. Kamrath, M. Z. & Rizzo, T. R. Combining Ion Mobility and Cryogenic Spectroscopy for Structural and Analytical Studies of Biomolecular Ions. *Acc. Chem. Res.* **51**, 1487–1495 (2018).
23. Voronina, L. *et al.* Conformations of Prolyl-Peptide Bonds in the Bradykinin 1-5 Fragment in Solution and in the Gas Phase. *J. Am. Chem. Soc.* **138**, 9224–9233 (2016).
24. Voronina, L., Scutelnic, V., Masellis, C. & Rizzo, T. R. Can Mutational Analysis Be Used to Assist Structure Determination of Peptides? *J. Am. Chem. Soc.* **140**, 2401–2404 (2018).
25. Scutelnic, V. *et al.* The Structure of the Protonated Serine Octamer. *J. Am. Chem. Soc.* **140**, 7554–7560 (2018).
26. Daly, S., MacAleese, L., Dugourd, P. & Chirot, F. Combining Structural Probes in the Gas Phase - Ion Mobility-Resolved Action-FRET. *J. Am. Soc. Mass Spectrom.* **29**, 133–139 (2018).
27. Daly, S. *et al.* Conformational changes in amyloid-beta (12-28) alloforms studied using action-FRET, IMS and molecular dynamics simulations. *Chem. Sci.* **6**, 5040–5047 (2015).
28. Daly, S. *et al.* Action-FRET: Probing the molecular conformation of mass-selected gas-phase peptides with förster resonance energy transfer detected by acceptor-specific fragmentation. *Anal. Chem.* **86**, 8798–8804 (2014).
29. Wu, R. *et al.* Structural Studies of a Stapled Peptide with Native Ion Mobility-Mass Spectrometry and Transition Metal Ion Förster Resonance Energy Transfer in the Gas Phase. *J. Am. Chem. Soc.* **144**, 14441–14445 (2022).
30. Shvartsburg, A. A. *Differential Ion Mobility Spectrometry*. (CRC Press, 2008). doi:10.1201/9781420051070
31. Walker, S. W. C. *et al.* Determining molecular properties with differential mobility spectrometry and machine learning. *Nat. Commun.* **9**, 5096 (2018).
32. Wu, R. *et al.* Rapid Differentiation of Asian and American Ginseng by Differential Ion Mobility Spectrometry-Tandem Mass Spectrometry Using Stepwise Modulation of Gas Modifier Concentration. *J. Am. Soc. Mass Spectrom.* **30**, 2212–2221 (2019).
33. Wu, R. *et al.* Fine adjustment of gas modifier loadings for separation of epimeric glycopeptides using differential ion mobility spectrometry mass spectrometry. *Rapid Commun. Mass Spectrom.* **34**, (2020).
34. Ruskic, D., Klont, F. & Hopfgartner, G. Clustering and Nonclustering Modifier Mixtures in Differential Mobility Spectrometry for Multidimensional Liquid Chromatography Ion Mobility–Mass Spectrometry Analysis. *Anal. Chem.* **93**, 6638–6645 (2021).
35. Levin, D. S., Vouros, P., Miller, R. A., Nazarov, E. G. & Morris, J. C. Characterization of Gas-Phase Molecular Interactions on Differential Mobility Ion Behavior Utilizing an Electrospray Ionization-Differential Mobility-Mass Spectrometer System. *Anal. Chem.* **78**, 96–106 (2006).
36. Ruskic, D. & Hopfgartner, G. Modifier Selectivity Effect on Differential Ion Mobility Resolution of Isomeric Drugs and Multidimensional Liquid Chromatography Ion Mobility Analysis. *Anal. Chem.* **91**, 11670–11677 (2019).
37. Tiwari, P., Wu, R., Metternich, J. B. & Zenobi, R. Transition Metal Ion FRET in the Gas Phase: A 10–40 Å Range Molecular Ruler for Mass-Selected Biomolecular Ions. *J. Am. Chem. Soc.* **143**, 11291–11295 (2021).
38. Bohnhorst, A., Kirk, A. T., Berger, M. & Zimmermann, S. Fast Orthogonal Separation by Superposition of Time of Flight and Field Asymmetric Ion Mobility Spectrometry. *Anal. Chem.* **90**, 1114–1121 (2018).
39. Anderson, A. G. *et al.* DMS-IMS2, GC-DMS, DMS-MS: DMS hybrid devices combining orthogonal principles of separation for challenging applications. *Chem. Biol. Radiol. Nucl. Explos. Sens. IX* **6954**, 69540H (2008).
40. Hudgins, R. R., Ratner, M. A. & Jarrold, M. F. Design of Helices That Are Stable in Vacuo. *J. Am. Chem. Soc.* **120**, 12974–12975 (1998).
41. Kohtani, M. & Jarrold, M. F. Water molecule adsorption on short alanine peptides: How short is the shortest gas-phase alanine-based helix? *J. Am. Chem. Soc.* **126**, 8454–8458 (2004).
42. Rossi, M. *et al.* Secondary structure of Ac-Alan-LysH+ polyalanine peptides (n = 5,10,15) in vacuo: Helical or not? *J. Phys. Chem. Lett.* **1**, 3465–3470 (2010).
43. Hoffmann, W. *et al.* Assessing the stability of alanine-based helices by conformer-selective IR spectroscopy. *Phys. Chem. Chem. Phys.* **18**, 19950–19954 (2016).
44. D.A. Case, H.M. Aktulga, K. Belfon, I.Y. Ben-Shalom, S.R. Brozell, D.S. Cerutti, T.E. Cheatham, III, G.A. Cisneros, V.W.D. Cruzeiro, T.A. Darden, R.E. Duke, G. Giambasu, M.K. Gilson, H. Gohlke, A.W. Goetz, R. Harris, S. Izadi, S.A. Izmailov, C. Jin, K. Ka, and P. A. K. Amber 2021. (2021).
45. Bekker, H.; Berendsen, H.; Dijkstra, E.; Achterop, S.; Vondrumen, R.; Vanderspoel, D.; Sijbers, A.; Keegstra, H.; Renardus, M. In Gromacs-a Parallel Computer for Molecular-Dynamics Simulations. in *4th International Conference on Computational Physics (PC 92)* 252–256 (1993).
46. Berendsen, H. J.; van der Spoel, D.; van Drunen, R. Gromacs: A Message-Passing Parallel Molecular Dynamics Implementation. *Comput Phys Commun* **91**, 43–56 (1995).
47. Lindahl, E., Hess, B. & van der Spoel, D. GROMACS 3.0: A package for molecular simulation and trajectory analysis. *J. Mol. Model.* **7**, 306–317 (2001).
48. Maier, J. A. *et al.* ff14SB: Improving the Accuracy of Protein Side Chain and Backbone Parameters from ff99SB. *J. Chem. Theory Comput.* **11**, 3696–3713 (2015).
49. Liu, C. *et al.* Assessing Physicochemical Properties of Drug Molecules via Microsolvation Measurements with Differential Mobility Spectrometry. *ACS Cent. Sci.* **3**, 101–109 (2017).
50. Ieritano, C. *et al.* The Charge-State and Structural Stability of Peptides Conferred by Microsolvating Environments in Differential Mobility Spectrometry. *J. Am. Soc. Mass Spectrom.* **32**, 956–968 (2021).
51. Nguyen, C., Gilson, M. K. & Young, T. Structure and Thermodynamics of Molecular Hydration via Grid Inhomogeneous Solvation Theory. 1–16 (2011).
52. Nguyen, C. N., Kurtzman Young, T. & Gilson, M. K. Grid inhomogeneous solvation theory: Hydration structure and thermodynamics of the miniature receptor cucurbit[7]uril. *J. Chem. Phys.* **137**, 973–980 (2012).

Methods

Materials. Atto 532 with a maleimide linker was purchased from Atto-Tec (Siegen, Germany). Carboxyrhodamine 6G (crh6g) with a different maleimide linker length was purchased from Setareh Biotech (Oregon, USA). tmP1 (CAARAHAAAHARAARA), P1 (CAAAHAAAHAAAAHAAAHAAACAK), and P2 (KACAAAHAAAHAAAAHAAAHAAAC), with N-terminal acetylation and C-terminal amidation, were purchased from GenScript Biotech (Leiden, Netherland). tmP2 ($C_2H_3H_7$, ACHAAKHAKAAAAAKA), tmP3 ($C_2H_6H_{10}$, ACAAKHAAKHAAAAKA), and tmP4 ($C_2H_{10}H_{14}$, ACAAKAAAKHAAAHKA) are rhodamine 110 dye-labeled peptides, which were commercially obtained (Thermo Fisher Scientific, USA) in lyophilized form, with N-terminal acetylation and C-terminal amidation. Rhodamine 110 (rh110) was labeled to cysteine (Cys2) using a C6-maleimide linker. The labeling processes were also performed for cR6G-tmP1, P1-Atto 532, cR6G-P1-QSY7, and cR6G-P2-QSY7, according to an established protocol.[53] Briefly, to label cysteine groups with maleimide dyes, a reduction of the cysteine residue was performed using dithiothreitol (DTT). The excess DTT was removed by HPLC purification and the peptide lyophilized. The peptide powder was dissolved in 100 mM potassium phosphate buffer (pH = 7.1 for maleimide) at a concentration of approximately 2 mg/mL, and reactive dye with a maleimide linker was dissolved in DMF at a concentration of 10 mg/mL. Reactive dye solution (20 μL) was added to the sample solution, slowly vortexed, and incubated for 1 hour with ice cooling. Finally, the sample was purified using an HPLC equipped with a UV/Vis detector. Fully/partially separated components were collected and then lyophilized. Aliquots of the samples were analyzed by mass spectrometry (i.e., exact mass measurement and collision-induced dissociation, CID) to verify the identity of the labeling products. The dye-labeled biomolecules were dissolved in water and analyzed by UV/Vis spectroscopy at 522 nm (cR6G), 532 nm (Atto 532), and 560 nm (QSY7) to determine the quantity. The molar extinction coefficient (ε) in H_2O for each dye are 94000, 115000, and 90000, respectively. Then samples were lyophilized again for storage. Before analysis, the samples were dissolved in water, and adjusted to a concentration of ~10-20 μM. The structure of samples used in this work are shown in Scheme S1.

DMS instrumentation and experiments. In DMS, the ions are transported by a carrier gas orthogonal to a varying alternating current electric field, which is usually called as dispersion field. The peak-to-peak voltage of dispersion field is called dispersion voltage (DV). Depending on the differential mobility (ΔK) of the ion, a net-movement of ion beam towards one of the electrodes results. By application of a direct current voltage, called as compensation voltage (CV) to one of two parallel electrodes, ions with a specific ΔK are stabilized and emitted from the DMS device. During the separation, other ions would collide with one of the electrodes and consequently discharge. DMS separation can be tuned by the electric field strength (dispersion voltage, DV), residence time, carrier gas composition, and gas modifier (type and concentration).[32,34,36,54] Gas modifiers in DMS separations are designed to mix with the carrier gas and influence the ion transport via cluster formation. The gas modifier concentration is crucial, likely resulting from the rate of clustering/ declustering and the ion-modifier binding energy.[32–36] The interaction between the ion and gas modifier molecule(s) are qualitatively displayed as their shift of CV. DMS separation is related with many physicochemical properties of ions, including microsolvation, CCS, and pK_a.[31,55] Direct calculation of CCS values from DMS data is possible for low m/z metabolites using machine learning.[56,57] DMS is also a highly mobile device that can be easily coupled to IM-MS for arrival time distribution measurements, which enable the CCS measurements.[58,59]

In this study, a home-built nanoelectrospray ionization (nanoESI or nESI) DMS device (see Figure S13) modified from a previous design was used.[60] Briefly, a nanoESI source was mounted inside an aerodynamic optimized polyether ether ketone (PEEK) housing (housing 1), whose design was inspired by the CaptiveSpray source (Bruker). The nanoESI source was connected to a counter electrode with a 2.0 mm i.d. skimmer. The counter electrode was grounded during the experiments. After passing through the skimmer, the ion cloud was focused through a second circular channel (~3 mm in axial direction, housing 2) and then entered the parallel DMS electrodes. Nebulizer gas (~1.1 L/min) was introduced into housing 1 to assist the nanoESI spray. Auxiliary gas (~0.1 L/min) was introduced into housing 2 to focus the ion cloud and increase the ion transmission. The nebulizer gas and auxiliary gas mix together and are served as the carrier gas between DMS electrodes. The DMS setup comprises two hemispherical electrodes made of stainless steel and fixed towards a cylindrical PEEK housing (housing 3). The resulting dimensions of the DMS cell were 30 × 10 × 1.0 mm (length × width × gap height). The DMS device was fixed onto a 3D translation stage, and then aligned with different mass spectrometer inlet before the routine experiment. The interface between the DMS device and the mass spectrometer inlet was left open (with a distance of ~2 mm). Therefore, nebulizer gas and auxiliary gas (i.e., carrier gas), instead of the vacuum drag or throttle gas by an external pump, define the ion residence time. The ions were carried by the carrier gas to pass through the DMS device, which is different from other DMS setups (like SelexIon from AB Sciex and FAIMS Pro from Thermo Scientific). In this work, the ion residence time is around 15 ms on average.

The spray voltage was maintained at ~1.0 kV in general. The dispersion voltage (DV) was kept to 4.5 kV for all experiments. The ions could be scanned in a CV range of -100 V to 100 V (i.e., broadband scan mode) with a pre-defined step in the power supply (HV100-12, Stahl-electronics). A narrow CV range (narrowband scan mode) was usually applied to reduce the data acquisition time. LabVIEW scripts were programmed to synchronize the mass spectra acquisition and CV scan. In the gas modifier-assisted DMS experiments, a stepwise modulation of gas modifier concentration from 0 to 0.5 mol % was applied according to an established protocol.[32,33] Gas modifier, like isopropanol (IPA) or acetonitrile (ACN) solvent, was injected into a home-built porous *polytetrafluoroethylene* (PTFE) gas mixer. The gas mixer consists of a housing packed with multiple porous PTFE plates with a thickness of 2 mm each (HiPep Laboratories). The selection of the gas modifier and its concentration are still largely empirical for optimal separation of different analytes. It is worth to mention that a slight shift of the peak position in the resulting DMS ionogram is usually due to the fluctuation of modifier concentration and the asymmetric waveform (amplitude and shape). In this work, DMS was coupled with a modified quadrupole ion trap (QIT) MS for the gas-phase fluorescence spectroscopy experiments (i.e., emission spectroscopy and fluorescence lifetime). Moreover, DMS was also connected to a Synapt G2-S QTOF-MS for the tandem DMS–TWIM experiments.

Ion mobility mass spectrometry (IM-MS). In this work, IM-MS experiments were performed in a Synapt G2-S QTOF-MS (Waters). For the nanoESI experiment, 5 μL of 10-20 mM peptide sample was loaded into a ~1.5 mm i.d. pulled glass capillary (1.0 mm o.d., 0.75 mm i.d.). The glass capillary was pulled in house by a micropipette puller (P-1000, Sutter Instrument). The spray voltage (~1 kV) was applied via a platinum wire. For IM-MS measurements, corrected N_2 CCS values of ions were calculated by using poly-DL-alanine in the Major Mix IMS/Tof calibration kit as the calibrant, and calibration was fitted by linear fit method. 7.0 V, 7.5 V, and 8.0 V wave height voltage were applied to determine the variation of calibration. Some improved calibration approach could further reduce the uncertainty, such as a reported method with over 2500 experimental TWIM data sets.[61] The acquired Raw files were converted into mzxml format by MSConvert (ProteoWizard), further processed by Matlab scripts (R2021a, mathworks) to generate DMS ionogram. All data were then analyzed using OriginPro 2021 (OriginLab).

IM-MS experiments were also performed in a SELECT SERIES Cyclic IMS (cIM, Waters) for a better separation of P1-Atto 532 and

Atto 532-P1 mixture (Figure S21). Three peaks could easily be identified in the resulting ion mobility spectra with one or two passes in the cyclic IM . Conformer 4 was missing, which is likely due to a low concentration of P1-Atto 532 in the mixture sample used for cIM separation (refer to the discussion section of Figure 2 in the manuscript). Besides, differences could also result from the instrumental conditions (in terms of softness). Nevertheless, conformational and the CCS distributions for the $[M+3H]^{3+}$ ion of P1-Atto 532 in two IM-MS instruments were similar.

Fluorescence spectroscopic measurements. The instrumentation and methodology of mass-selected fluorescence measurements in the gas phase are described elsewhere.[19] Briefly, a quadrupole ion trap (QIT) MS was modified and coupled with tunable laser excitation and highly sensitive fluorescence detection systems. Gaseous ions, generated using nanoESI, are trapped in the QIT that allows optical access for laser irradiation. For the tmFRET experiments, 50-100 mM $CuCl_2$ in water was added into the peptide samples to form the copper adducted ions. Ions were accumulated for 1 s, and then trapped in the ion trap (q_z = 0.75). Mass isolation of 1 s was then conducted. Meanwhile, the trapped ions were irradiated for 1 s by a laser beam from a tunable Ti:Sapphire fs laser (MaiTai, Spectra-Physics, U.S.A.) at a wavelength of 460 nm and a laser power of ~10 mW. The helium buffer gas was injected into the trap to cool the ion packets and reduce the photodissociation (PD) due to laser irradiation. Mass spectra of isolated ions were acquired during the fluorescence measurements. Mass spectrometric data were recorded by LCQ Tune (Thermo Fisher). The emitted fluorescence was then collected from a 5.0 mm diameter hole drilled into the ring electrode of the QIT and is directed toward the detection setup. Around 1.8% of the emitted fluorescence reaches the detectors. The collected fluorescence was collimated and sent to the spectrograph with an electrothermally-cooled CCD. The time-resolved fluorescence measurement was performed with a Single-Photon Avalanche Diode (SPAD) using Time Correlated Single Photon Counting (TCSPC). Fluorescence spectra were recorded by Solis (version 4.3, Andor), lifetime decay curves were recorded by Time Harp software. All data were then analyzed using OriginPro 2021 (OriginLab).

Solution-phase FRET experiments of cR6G-P1-QSY7 and cR6G-P2-QSY7 (Figured S24-S25 and Table S9) were conducted in the home-built in-plume ESI setup.[59] As QSY7 is a dark quencher and could potentially undergo photobleaching, the experiments were conducted with freshly prepared samples in a low ~mW laser power and limited lifetime acquisition time.

Distance estimation from FRET efficiency (E_{FRET}). The methodology to estimate the FRET efficiency (E_{FRET}), Förster distance in the gas phase ($R_{0,gas}$), and distances of donor-acceptor distance (r_{DA}) were based on an established model from literature.[37,62] The donor (cR6G) emission and acceptor (QSY7) absorption spectra were acquired to calculate the spectral overlap (*J*) in the solution phase (Figure S31). Further, the quantum yield of donor dye (cR6G) in the solution (Φ = 0.63) was incorporated into the calculation.[63] The refractive index of water and vacuum were 1.33 and 1.0, respectively. In this work, *J* is =3.848*10^15 $nm^4/(M*cm)$, and the solution phase R_0 ($R_{0,solution}$) for cR6G and QSY7 was 59.7 Å. the gas phase R_0 ($R_{0,gas}$) was 72.2 Å. For tmFRET experiments, the excitation spectrum of cR6G and absorption spectrum of $CuCl_2$ solution in pH ~7 (Figure S31) was used to calculate *J*, which gave a value of $8.444*10^{12}$ $nm^4/(M*cm)$ in ae software (FluorTools). Therefore, $R_{0,gas}$ for cR6G and Cu^{2+} pair was determined to be 26.0 Å.

Lifetimes presented in this work were determined by fitting of the experimental data using a gaussian-modified exponential function (GaussMod or single-exponential fit). Here, we explored further possibilities, such as a multi-exponential decay using the DecayFit software (FluorTools, www.fluortools.com). The instrument response function (IRF) was obtained from the gaussian-modified exponential fit of a high signal-to-noise data set.

Force field parameters. The AmberTools21 simulation package[44] was used to prepare the peptide starting structures for subsequent simulations. Parameters for the chromophores were derived with the antechamber[64] module applying the AM1-BCC model[65,66] for partial charges and general amber force field 2[67] atom types. For the peptides' standard amino acid residues we assigned parameters according to the Amber force field 14SB.[48] Coordinate files and topologies were then generated with LeaP.

Conformational search. To efficiently sample a diverse conformational ensemble for each peptide, we employed an extensive simulated annealing protocol. In this protocol the temperature was elevated to 1500 K within 5000 simulation steps, from step 5001 to 400000 the peptide structure freely moved at 1500 K. The system was then cooled down again to 0 K from step 400001 to step 450000, where it was simulated for another 50000 simulation steps. The resulting conformation was then reused as starting structure for the another simulated annealing run. We first repeated this heating and cooling cycles to generate 100 conformations. From each of those structures we started 50 more simulated annealing cycles, thus totaling to 5000 conformations per peptide. For these 5000 final conformations we performed an additional energy minimization with a maximum of 5000 cycles, where the minimization algorithm switched from steepest descent to conjugate gradient after 1000 steps. The temperature in our simulations were regulated using the Langevin thermostat[68] implemented in the sander simulation engine. All bonds involving hydrogens were constrained using the SHAKE algorithm[69].

For subsequent microsolvation calculations, we refined the diverse conformational ensembles generated for each peptide based on the experimental CCS values and FRET distances as well as their force field energies (20% cutoff). The CCS values for each conformation were estimated using the ion mobility projection approximation calculation tool, IMPACT[70]. Distances between the dyes were calculated using cpptraj[71]. The refined 20 structures and their exact ranges for CCS values, FRET distances, and energies are shown in Figure S32 and Table S14.

Microsolvation calculations. To estimate the interaction potential of each peptide with acetonitrile, we derived favorable interactions sites using grid inhomogeneous solvation theory (GIST).[51,52] GIST was originally developed to calculate the interaction energies of biomolecular systems in explicit water simulations[72,73] and has recently been generalized for all rigid solvents.[47,74,75] The fundamental concept was to simulate the restrained peptide conformation in an explicit acetonitrile solvent box and subsequently evaluated all energetic contributions on a grid. Acetonitrile (ACN) concentration used during the DMS experiments was higher enough to allow sufficient molecules for clustering also in the simulation. For these restrained simulations we generated solvated coordinates and topologies for the selected conformations with a minimum wall distance of 3 nm. Simulations were then performed using the GROMACS 2020.5 simulation engine[45–47], using ParmEd to convert all required files. The acetonitrile solvent box was first minimized with the steepest descent algorithm for a maximum of 50000 minimization steps. To equilibrate the solvated system, we first heated up the system for 1 ps to 300 K in the NVT ensemble. Here we applied the LINCS[76] algorithm to constrain all bonds involving hydrogens to allow for a time step of 2 fs. We chose the particle mesh Ewald approach for the treatment of long-range electrostatic interactions and a cutoff distance of 1 nm for short range electrostatics and van der Waals interactions. For pressure equilibration 1 ns of simulation time was acquired using the Berendsen barostat[77] with a time constant of 2 ps to maintain atmospheric pressure. All following production runs were performed with the same conditions in the NPT ensemble using a force constant of 1000 kcal/mol per atom. For each conformation we collected a simulation time 50 ns.

The analysis of interaction energies using GIST was performed with the GPU-accelerated version of cpptraj.[78] A simulation of a pure acetonitrile solvent box was used to estimate to solvent-solvent interaction energy of acetonitrile (-7.006 kcal/mol). With

the gisttools analysis package we then generated density maps of the interaction energy for each conformation. We then identified the most probable microsolvation sites based on the areas with the lowest interaction energies considering only voxels with a interaction energy below -1.5 kcal/mol. Each of the identified sites was then used to guide the placement of explicit acetonitrile molecules in the modeling of the microsolvated complexes. We estimated the interaction energy of each conformation with acetonitrile as modifier molecule using the linear interaction energy scheme implemented in cpptraj.[71]

Data availability

All experimental details and data are available within the paper and supporting information. The original data used in this publication will be made available in a curated data archive at ETH Zurich (https://www.researchcollection. ethz.ch) under the DOI: 10.3929/ethz-b-000545943

References

53. Thermofisher. Amine-Reactive Probes | 2 Labeling Proteins. https://tools.thermofisher.com/content/sfs/manuals
54. Gabelica, V. *et al.* Recommendations for reporting ion mobility Mass Spectrometry measurements. *Mass Spectrom. Rev.* **38**, 291–320 (2019).
55. Campbell, J. L., Zhu, M. & Hopkins, W. S. Ion-Molecule Clustering in Differential Mobility Spectrometry: Lessons Learned from Tetraalkylammonium Cations and their Isomers. *J. Am. Soc. Mass Spectrom.* **25**, 1583–1591 (2014).
56. Ieritano, C., Campbell, J. L. & Hopkins, W. S. Predicting differential ion mobility behaviour: In silico using machine learning. *Analyst* **146**, 4737–4743 (2021).
57. Ieritano, C. *et al.* Determining collision cross sections from differential ion mobility spectrometry. *Anal. Chem.* (2021). doi:10.1021/acs.analchem.1c01420
58. Chingin, K. *et al.* Direct Access to Isolated Biomolecules under Ambient Conditions. *Angew. Chemie* **122**, 2408–2411 (2010).
59. Tiwari, P., Czar, M. F. & Zenobi, R. Fluorescence-Based Detection of the Desolvation Process of Protein Ions Generated in an Aqueous Electrospray Plume. *Anal. Chem.* **93**, 3635–3642 (2021).
60. Wu, R. *et al.* Performance Enhancements in Differential Ion Mobility Spectrometry-Mass Spectrometry (DMS-MS) by Using a Modified CaptiveSpray Source. *J. Am. Soc. Mass Spectrom.* **29**, 2199–2207 (2018).
61. Richardson, K., Langridge, D., Dixit, S. M. & Ruotolo, B. T. An Improved Calibration Approach for Traveling Wave Ion Mobility Spectrometry: Robust, High-Precision Collision Cross Sections. *Anal. Chem.* **93**, 3542–3550 (2021).
62. Czar, M. F. *et al.* Gas-Phase FRET Efficiency Measurements to Probe the Conformation of Mass-Selected Proteins. *Anal. Chem.* **87**, 7559–7565 (2015).
63. López Arbeloa, T., López Arbeloa, F., Hernández Bartolomé, P. & López Arbeloa, I. On the mechanism of radiationless deactivation of rhodamines. *Chem. Phys.* **160**, 123–130 (1992).
64. Wang, J., Wang, W., Kollman, P. A. & Case, D. A. Automatic atom type and bond type perception in molecular mechanical calculations. *J. Mol. Graph. Model.* **25**, 247–260 (2006).
65. I, A. C. A. M., Jakalian, A., Bush, B. L., Jack, D. B. & Bayly, C. I. Fast, Efficient Generation of High-Quality Atomic Charges. AM1-BCC Model: I. Method. **21**, 132–146 (1999).
66. Jakalian, A., Jack, D. B. & Bayly, C. I. Fast, efficient generation of high-quality atomic charges. AM1-BCC model: II. Parameterization and validation. *J. Comput. Chem.* **23**, 1623–1641 (2002).
67. Wang, J., Wolf, R. M., Caldwell, J. W., Kollman, P. A. & Case, D. A. Development and testing of a general Amber force field. *J. Comput. Chem.* **25**, 1157–1174 (2004).
68. Adelman, S. A. & Doll, J. D. Generalized Langevin equation approach for atom/solid-surface scattering: General formulation for classical scattering off harmonic solids. *J. Chem. Phys.* **64**, 2375–2388 (1976).
69. Ryckaert, J. P., Ciccotti, G. & Berendsen, H. J. C. Numerical integration of the cartesian equations of motion of a system with constraints: molecular dynamics of n-alkanes. *J. Comput. Phys.* **23**, 327–341 (1977).
70. Marklund, E. G., Degiacomi, M. T., Robinson, C. V., Baldwin, A. J. & Benesch, J. L. P. Collision Cross Sections for Structural Proteomics. *Structure* **23**, 791–799 (2015).
71. Roe, D. R. & Cheatham, T. E. PTRAJ and CPPTRAJ: Software for processing and analysis of molecular dynamics trajectory data. *J. Chem. Theory Comput.* **9**, 3084–3095 (2013).
72. Nguyen, C. N., Cruz, A., Gilson, M. K. & Kurtzman, T. Thermodynamics of water in an enzyme active site: Grid-based hydration analysis of coagulation factor xa. *J. Chem. Theory Comput.* **10**, 2769–2780 (2014).
73. Ramsey, S. *et al.* Solvation thermodynamic mapping of molecular surfaces in ambertools: GIST. *J. Comput. Chem.* **37**, 2029–2037 (2016).
74. Kraml, J. *et al.* Solvation Thermodynamics in Different Solvents: Water-Chloroform Partition Coefficients from Grid Inhomogeneous Solvation Theory. *J. Chem. Inf. Model.* **60**, 3843–3853 (2020).
75. Waibl, F. *et al.* Grid inhomogeneous solvation theory for cross-solvation in rigid solvents. *J. Chem. Phys.* **156**, (2022).
76. Hess, B., Bekker, H., Berendsen, H. J. C. & Fraaije, J. G. E. M. LINCS: A Linear Constraint Solver for molecular simulations. *J. Comput. Chem.* **18**, 1463–1472 (1997).
77. Berendsen, H. J. C., Postma, J. P. M., Van Gunsteren, W. F., Dinola, A. & Haak, J. R. Molecular dynamics with coupling to an external bath. *J. Chem. Phys.* **81**, 3684–3690 (1984).
78. Kraml, J., Kamenik, A. S., Waibl, F., Schauperl, M. & Liedl, K. R. Solvation Free Energy as a Measure of Hydrophobicity: Application to Serine Protease Binding Interfaces. *J. Chem. Theory Comput.* **15**, 5872–5882 (2019).

Acknowledgments

The authors are grateful to the Swiss National Science Foundation (grants number 200020_207354 and 200020_178765) and ETH Zürich (grant ETH-07 15-1) for funding. J. B. Metternich are grateful towards the Fonds der Chemischen Industrie for generous financial support (Kekulé scholarship) and A. S. Kamenik gratefully acknowledges funding by the Austrian science fund via a Schrödinger Fellowship (J 4569). We also thank LOC mechanical workshop for technical support.

Author Contributions

R.W., J.B.M., and A.S.K. contributed equally. R.W. designed the research, performed all DMS, IM-MS, fluorescence measurements, and analyzed the data. R.W. and R.Z. wrote the manuscript with input from all authors. J.B.M. conducted peptide synthesis and contributed to TWIM-CID studies. A.S.K. and S.R. conducted conformational search and microsolvation studies. P.T. contributed to the tmFRET studies. J.A.H. contributed to IM-MS studies. R.W., D.K., and H.A. collected preliminary DMS and fluorescence data of P1-Atto 532. L.R.B. contributed to solution-phase lifetime measurements. T.W.D.C contributed to the DMS instrumentation and measurements. All authors have given approval to the final version of the manuscript.

Competing Interests

The authors declare no competing financial interest.

Additional information

Supporting Information. The Supporting Information is available free of charge via the Internet at:

Table of Contents (TOC)